Modeling Of Copper Diffusion In Amorphous Aluminum Oxide in CBRAM Stack

K. Sankaran[a,b], L. Goux[a], S. Clima[a], M. Mees[a,c], J. Kittl[a], M. Jurczak[a], L. Altimime[a], G.-M. Rignanese[b] and G. Pourtois[a,d]

[a] imec, Kaperldreef 75, B-3001 Leuven, Belgium
[b] European Theoretical Spectroscopy Facility (ETSF) and Institute of Condensed Matter and Nanosciences (IMCN), Université Catholique de Louvain, Chemin des Étoiles 8, B-1348 Louvain-la-Neuve, Belgium
[c] Department of Physics, Katholieke Universiteit Leuven, Celestijnenlaan 200 D, B-3001 Leuven, Belgium
[d] PLASMANT, University of Antwerp, Universiteitplein, B-2610 Wilrijk-Antwerp, Belgium

First-principles modeling techniques are used to study the diffusion of copper in amorphous alumina (a-Al_2O_3) for Conductive Bridging Random Access Memories (CBRAM) Pt/$Cu_xTe_{(1-x)}$/Al_2O_3/Si stacks. The enthalpy of injection (E_i) of $Cu^{(+1/+2)}$ and $Te^{(-2/+2)}$ ions into a-Al_2O_3 have been quantified. We found that the kinetics associated to Cu^{+1} injection is characterized by a diffusion pre-factor of 5.8×10^{-4} cm^2/s and an activation energy of 0.9 eV in a-Al_2O_3. The diffusion kinetics of the Te^{+2} ions is similar to the Cu^{+1} one.

Introduction

The downscaling of the physical dimensions of electronic devices is driven by the need to develop improved functionalities with reduced production cost. In such a context, the increasing demand for non volatile memory for application in PC tablets and smart phones is pushing the industries to develop large storage capacity memories. One of the main hurdles consists in reaching performances similar to the conventional floating gate based flash memories. Many alternative technologies have been developed (1). Among them, resistive switching based memories are currently the object of intense investigations. Resistive switching effects can originate from numerous physical mechanisms, including thermal (phase change, fuse/anti-fuse), electronic (charge trap/injection, ferroelectric), magnetic (anisotropic/giant magneto resistance, spin torque transfer switching), or ionic (cation/anion migration) effects (1).

Among the different types of resistive switching based memories, the ionic migration based Conductive Bridging Random Access Memory (CBRAM) is a very attractive concept. It offers an excellent scaling potential, endurance-robustness and low power operability (2, 3). Its working principle consists in injecting metal ions (typically Cu and Ag) into a solid electrolyte upon the application of a voltage. The metal ions are accumulated to form a thin conductive nanofilament between the electrodes. The resistance of the cell is thus dominated by the low resistive state metallic bridge (ON-

state) or by the high resistive one, whenever the nanofilament is disrupted (OFF-state), enabling the storage of data bits.

Originally, chalcogenides such as GeSe or GeS were used as solid electrolytes due to the high diffusivity of Cu or Ag in these materials (2-4). However, a too high diffusivity affects the stability of the bridge and results into low switching voltage (V_{sw}) that cannot be reproducibly controlled through a read/write cycling of the stack (2-4). As an alternative, binary oxide materials such as Ta_2O_5 (5,6) or GdO_x (7) have been introduced, but they require a higher reset current (I_{reset}) compared to the chalcogenides (5,6).

It has been shown that a CMOS-compatible CBRAM stack (Figure 1a) built from an amorphous aluminum (a-Al_2O_3) sandwiched between a Si n+ substrate and a Cu_xTe_{1-x} alloy contacted by a Pt metal electrode could offer an excellent trade-off between I_{reset} and V_{sw} together with good retention characteristics (8). The main role of the Cu_xTe_{1-x} layer is to act as a Cu cation source. Cu ions migrate into the solid electrolyte of a-Al_2O_3 to form the nanofilament, while the other layers of Si n+ and Pt are contact electrodes. In order to get a Cu cations supply from Cu_xTe_{1-x}, a composition ranging between $0.5 < x < 0.7$ is needed (8). This composition is particularly interesting for the self limitation of the filament formation, which does not require a current limiter, and thus allows a good controllability and low I_{reset} characteristics (8).

Although the working principle of this stack is known (Figures 1b and 1c), the atomistic switching mechanism is still the object of a large debate. Moreover, the detailed physical parameters on which the device is built remain unclear. The thermodynamics and the kinetic aspects of Cu cations injection in the a-Al_2O_3 are therefore of fundamental importance. In this framework, atomistic modeling techniques, based on Density Functional Theory (DFT) are choice tools to quantify the physical parameters of the ionic diffusion in these materials, namely the injection energies (E_i), diffusion pre-factor (D_0) and activation energy (E_a). Through this paper, we will present the modeling efforts undertaken to understand the physical properties and parameters of the materials used in this CBRAM stack. The kinetic aspects of the ionic diffusion are quantified using accelerated ab initio molecular dynamics (AIMD) based on the bond boosted technique (9).
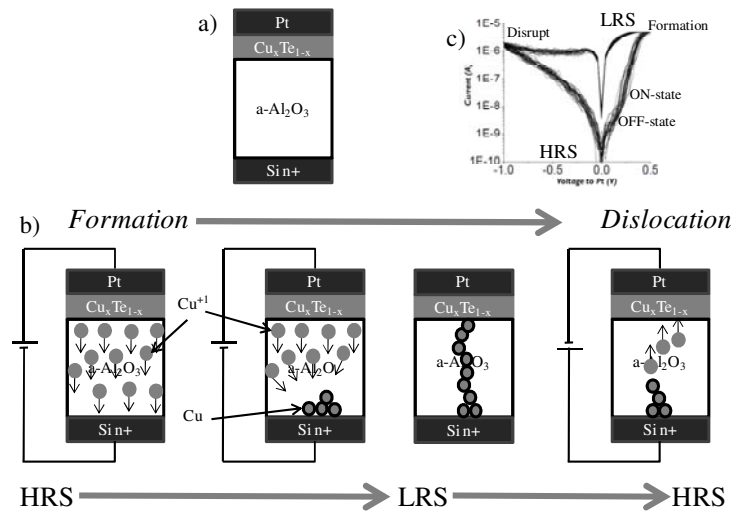
Figure 1. Schematic illustration of a CBRAM stack (a), together with its working principles upon the application of a voltage (b) and the consecutive I-V cycles obtained using a programming current (c).

Methodology

Computation of the amorphous model (a-Al_2O_3)

A model structure of a-Al_2O_3 has been generated using a classical molecular dynamics approach (MD) relying on the empirical pair potentials developed by Buckingham (10). A melt-and-quench treatment (11) has been coupled to a NPT thermostat with a time step interval of 1 fs. As a starting point, we used an orthorhombic crystal of γ–Al_2O_3 with a density of 3.1 g/cm^3 as a start structure. This initial structure (containing 160 atoms) is heated up to 4000K and thermalized for 50 000 time steps. The molten structure is then equilibrated at 4000K and linearly cooled down to 300K with a constant cooling rate of 5.5×10^{14} K/s. Once 300K is reached, the system is again equilibrated for more than 50 000 time steps.

The resulting atomic positions are then relaxed using DFT until all atomic forces lie below 2.6×10^{-3} eV/Å (Figure 2a). The exchange-correlation energy is approximated using the Perdew-Berke-Ernzenof (PBE) functional (12). All the simulations have been carried out using Vanderbilt ultra-soft pseudopotentials (13) as implemented in Quantum-Espresso package (14). A convergence of the total energy of 10^{-5} eV is guaranteed with a kinetic energy cut-off of 340 eV and a 2x2x2 Monkhorst-pack grid of k-points to sample the Brillouin zone.
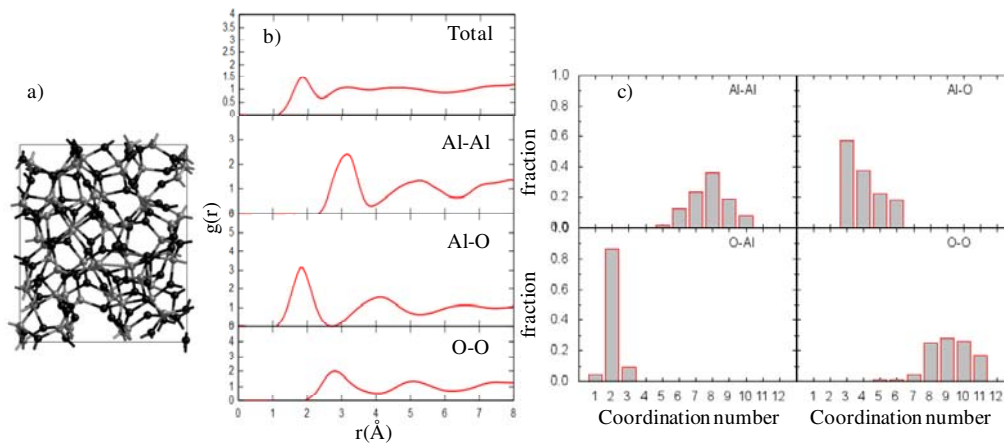
Figure 2. (a) Illustration of the amorphous model structure of Al_2O_3 generated with 64 Al atoms (grey) and 96 O atoms (black). (b) Total and partial pair-distribution functions for a-Al_2O_3. (c) Distribution of the Al and O nearest neighbor-coordination in a-Al_2O_3.

In order to determine the accuracy of the generated a-Al_2O_3 model, we compare its structural properties, such as the radial pair-distributions (RDP) and the coordination numbers with literature (15). The degree of disorder obtained for our a-Al_2O_3 is comparable to the one reported in Ref (15). The RDP generated for a-Al_2O_3 are shown in Figure 2b. A main peak is present at 1.8 Å and corresponds to Al-O bonds and two minor ones are located at 3.0 and 2.8 Å and represent the Al-Al and O-O bonds, respectively. The computed nearest-neighbors coordination numbers of a-Al_2O_3 matches the ones reported for model "E" in Ref (15) for a density of 3.1 g/cm^3 (Table I).

TABLE I. Structural and electronic properties of a-Al_2O_3 compared with Ref(14) and experimental values.

	Unit cell (Å)	ρ (g/cm^3)	Band gap (eV)
Our model	12.0×10.4×14.3	3.1	3.4
Other theoretical model(15)	9.27×7.29×9.70	3.1	3.6
Expt. (16-17)	-	-	5.1-6.9

Computation of injection energies

To determine the most stable ionic oxidation state in a-Al_2O_3, we calculate the injection energies, E_i, for the insertion of a Cu or a Te ion into a-Al_2O_3. E_i is a function of the Fermi level ε_f whose position is used as variable and depends on the valence band offset ε_v according to the following formula [1]:

$$E_i(\alpha, q) = E(\alpha, q) - (E_0 + n_\alpha \bullet \mu_\alpha) - q \bullet (\varepsilon_F + \varepsilon_v) + E_{corr} \qquad [1]$$

where E_0 is the total energy of a non defective a-Al_2O_3 and n_α is the number of Cu/Te ions added to the supercell with its chemical potential μ_α. ε_F varies within the edges of the

band gap. Note that, the measured experimental band gap fluctuates between 5.1 and 6.9 eV (Table I). This will impact the position of the Fermi energy at equilibrium, and hence limit any comparison with the experimental forming/set and reset voltage of Ref (8). E_{corr} is a correction term that accounts for the spurious interaction of the charge defect with its images in the neighboring cells when periodic boundary conditions are applied (18). In this case, E_{corr} is estimated to vary from 0.1 to 0.4 eV for an ionic charge (q) ranging from -2 to +2.

Computation of the diffusion coefficients of Cu/Te ions in a-Al_2O_3

The kinetics parameters such as the diffusion coefficients of Cu/Te in a-Al_2O_3 are investigated by performing a series of accelerated AIMD using the bond-boosted technique developed by Miron *et al.* (9) with a canonical Nosé thermostat (19) and a 1 fs time step. This technique consists of adding a repulsive potential to each bond belonging to a 'boosted atomic region' to induce either their compression or stretching with respect to their equilibrium value. As a result, the deformed bonds favor a transition from different minima of the potential energy surface. The gain in time is proportional to the exponential of the applied potential. This method offers the possibility to observe infrequent events that occur at the atomic scale at a tractable computational cost. The computation of the atomic forces and total energies have been carried out with the Siesta DFT package (20) using the PBE exchange correlation functional (12) combined with a localized basis set of a double zeta type and Norm conserving pseudopotentials (21).

In this framework, the diffusion coefficient is bound to the spatial motion of the particles embedded in the statistically averaged mean square displacement (MSD), defined by the Einstein relation. On the basis of the MSD, the self diffusion coefficient D is derived as:

$$D = \lim_{t\to\infty} 1/(6 \cdot t) \; < [\; r(t+t_0) - r(t_0) \;]^2 > \; \equiv \lim_{t\to\infty} 1/(6 \cdot t) < [\; r(t) - r(0) \;]^2 > \quad [2]$$

where t or t_0 is the time and r(t) is the ion site at arbitrary time t. For t large enough, a good approximation of the diffusion coefficient can be obtained. This is made possible thanks to the extended time scale reached with the AIMD technique. The diffusion coefficient is evaluated by AIMD at several temperatures i.e. 1400, 1200, 1000, 800, 600 and 400K without the application of any external bias. Such a thermal treatment is not large enough to induce a possible recrystallization of a-Al_2O_3. The temperature dependence of D exhibits an Arrhenius-type function behavior:

$$D = D_0 \cdot \exp[\; -E_a / (\; k_B \cdot T) \;] \quad\quad\quad [3]$$

where D_0 is the diffusion pre-factor, E_a is the activation energy, k_B is the Boltzmann constant and T is the temperature. Using an exponential fit of the D at different temperatures, it is possible to evaluate the intrinsic key parameters characterizing the electrolyte such as D_0 and E_a. Note that we mainly focus on the diffusion events that occur when no electric field is applied to the CBRAM stack. The applied electric field is

considered as being uniform over the stack at a given voltage and it is proportional to the thickness of the oxide. The work induced by the motion of a charged particle in uniform electric field alters the activation energy (an additional constant energy is simply added to the original value of E_a). Consequently, the potential surface energy is lowered and D is boosted. Subsequently, even though an electric field is applied, D_0 and E_a remain the key parameters to be determined.

Formation energies of extrinsic ions in a-Al$_2$O$_3$

The diffusion of ions in a-Al$_2$O$_3$ is controlled by the thermodynamics of their injection in the electrolyte. Therefore, these quantities need to be estimated. Figures 3 and 4 show the evolution of the injection energies of Cu and Te in their different ionic states with respect to the position of the Fermi level (ε_F). Note that the valence band alignment used depends strongly on the value of band gap used. We illustrate this dependence in Figures 3 and 4 for the extremes of the distribution reported in literature, i.e. band gaps of 5.1 (16) and 6.9 eV (17) (Table I). In our model of the Pt/Cu$_x$Te$_{1-x}$/a-Al$_2$O$_3$/Si stack, the Cu$_x$Te$_{x-1}$ acts as an ion source. As a result, both the Cu and Te ions might penetrate a-Al$_2$O$_3$. Experimentally, the proportion of Cu in Cu$_x$Te$_{1-x}$ varies between 50 and 70% (0.5<x<0.7) to favor the injection of Cu^{+1} ions (8). However, one cannot a priori rule out the possibility of injecting other oxidation stages or other ionic species. As a consequence, we studied the injection energies of Cu and Te with an ionic charge (q) varying from -2 up to +2. Interestingly, not all the degrees of oxidation are thermodynamically favored for the injection of Cu and Te in a-Al$_2$O$_3$ (Figures 3 and 4).
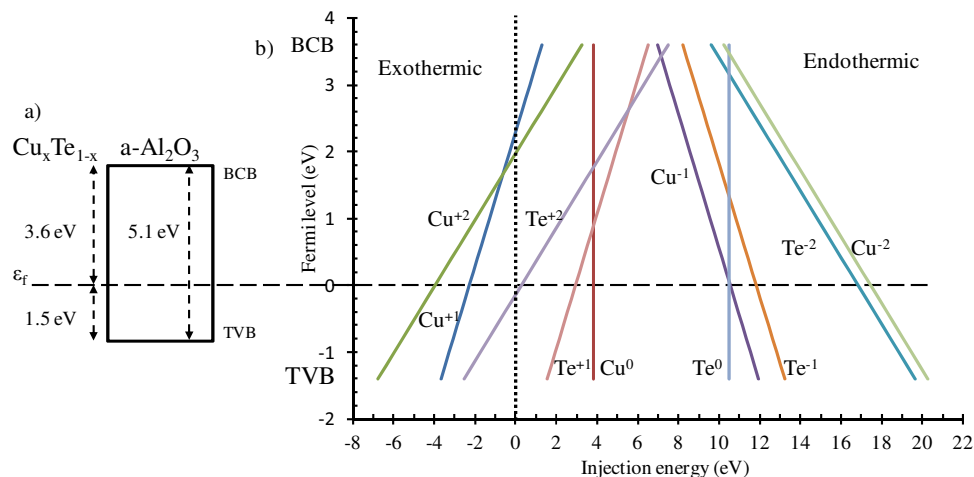
Figure 3. a) Flat band diagram of Cu$_x$Te$_{1-x}$ aligned with a-Al$_2$O$_3$ at the Fermi level   with a valence band offset of 1.5 eV (21). b) The evolution of the energies of injection of Cu and Te ions in a-Al$_2$O$_3$ with respect to the position of the Fermi level in the band gap of 5.1 eV of a-Al$_2$O$_3$ is delimited by the bottom of the conduction (BCB) and the top of the valence band (TVB). The dotted line separates the exothermic regime to the endothermic one.
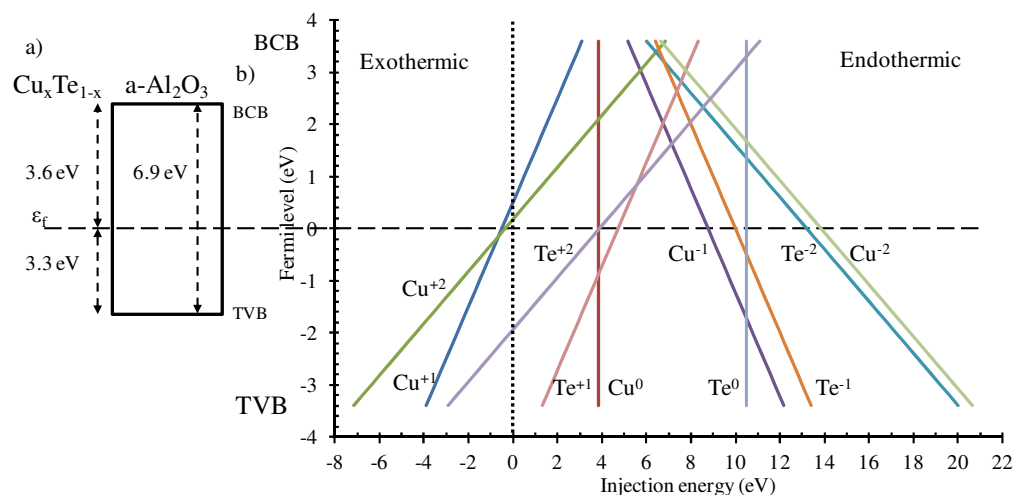
Figure 4. a) Flat band diagram of Cu_xTe_{1-x} aligned with a-Al_2O_3 at the Fermi level with a valence band offset of 3.3 eV (22). b) The evolution of the energies of injection of Cu and Te ions in a-Al_2O_3 with respect to the position of the Fermi level in the band gap of 6.9 eV of a-Al_2O_3 delimited by the bottom of the conduction (BCB) and the top of the valence band (TVB). The dotted line separates the exothermic regime to the endothermic one.

Equation [1] indicates that the energy required for the ion injection and consequently the solubility of the metal ions, is sensitive to the atomic chemical potential, as well as to the Fermi level. The latter takes into account the exchange between the host (a-Al_2O_3) and the chemical reservoir (Cu_xTe_{1-x}). Therefore, $E_i(Cu, +1)$ is mainly dependent on the chemical potential of Cu coming from Cu_xTe_{1-x} and this is also the case for Te. We fixed the Cu stoichiometry (x) to be 0.6 and the values of the chemical potential of Cu and Te sources accordingly to Ref (8). Moreover, the variation of the Cu stoichiometry (x), defined to evolve between 0.5 and 0.7, has no major influence on the chemical potential of Cu and Te (not shown here).

The lower and upper limits of the ε_F are set by the top of valence band (TVB) and bottom of conduction band (BCB), which corresponds to band gaps of a-Al_2O_3 (5.1 (16) – 6.9 eV (17)). Given the conduction band offset of 3.6 eV (22), between Cu_xTe_{1-x} and a-Al_2O_3, the distribution of the band gaps affects the definition of the position of the Fermi level at equilibrium and hence influences the oxidation degree of the injected ions. Assuming a band gap of 6.9 eV leads to a valence band offset of 3.3 eV (Figure 4.a). In this case, the application of a positive forming voltage will induce the injection of Cu^{+1} and Cu^{+2} only. At higher voltage (around 2.0 eV), the injection of Te^{+2} gets thermodynamically favored. On the other hand, a band gap of 5.1 eV shifts the equilibrium Fermi level at 1.8 eV lower in energy (Figure 3.a) which also favors the injection of Te^{+2} at lower voltage (Figure 3.b). This qualitative picture implies that Cu^{+1}, Cu^{+2} and Te^{+2} can be injected into a-Al_2O_3. However, the stoichiometry of Cu_xTe_{1-x} (with $0.5 < x < 0.7$) guaranties the predominance of Cu^{+1} over its Cu^{+2} (Te^{-2}) form. As a consequence, it is expected to control the bridging operation of the CBRAM.

Diffusion kinetics of Cu/Te ions in a-Al$_2$O$_3$

The thermodynamic and stoechiometric considerations suggest that the operation of CBRAM is mainly driven by the injection of Cu^{+1}. In order to gain deeper insight into the switching mechanism, we focus in this section on the determination of the kinetic aspects of the diffusion.

Diffusion of Cu ions

As detailed in the methodology section, each AIMD simulation that occurs at a defined temperature results in a specific ionic trajectory. Based on these trajectories, we compute the Mean Squared Displacement (MSD) related to the diffusion of Cu^{+1} (Figure 5). Note that due the stochastic nature of the events, the distribution of the error is cumulative and turns relatively large for the time window (t) modeled. Finally, the MSD collected at different temperatures are fitted with a linear regression to extract the diffusion coefficients (Table II) of the process, see equation [2].
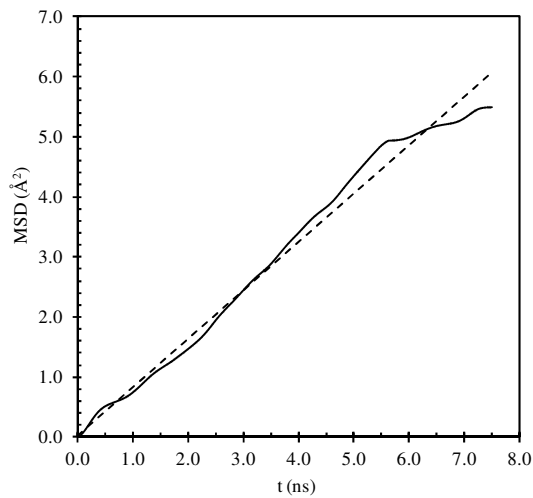
Figure 5. Mean square displacement of a Cu^{+1} ion into a-Al$_2$O$_3$ at 800K (solid line) and its corresponding linear regression fit (dotted line).

Table II. Computed diffusion coefficient from equation [2] for a Cu^{+1} in a-Al_2O_3.

T [K]	D (cm^2/s)
1400	1.03×10^{-6}
1200	1.38×10^{-6}
1000	1.9×10^{-7}
800	2.44×10^{-9}
600	1.27×10^{-10}
400	3.93×10^{-14}

Table II shows the evolution of the computed diffusion coefficients with respect to the temperature (equation [2]).
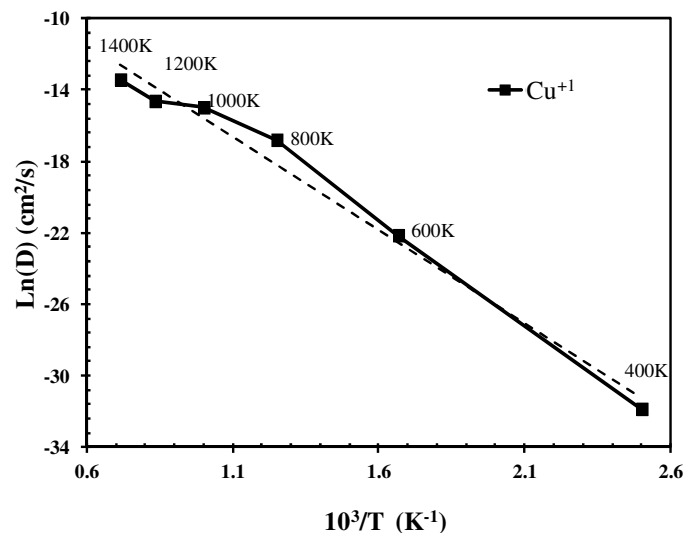
Figure 6. Temperature dependence of the diffusion coefficient of Cu^{+1} interstitial in a-Al_2O_3 (solid line) and its linear regression fitting (dotted line).

Figure 6 shows the data points from Table II for Cu^{+1} in a semi-logarithm scale. The diffusion pre-factor and the activation energy extracted from the linear regression (see Equation (3)) are 5.8×10^{-4} cm^2/s and 0.90 eV, respectively. Unfortunately, no literature values are available for comparison. These values however correlate with the one obtained by programming pulse width (electrical measurement) techniques on this CBRAM stack (22).

Interestingly, the analysis of the trajectory of the Cu^{+1} ion reveals that the interstitial Cu^{+1} ion jumps between two different low atomic density regions (cavity) within a-Al_2O_3. This hopping process is facilitated by the distribution of the free electron pairs of the oxygen atoms that attract the Cu^{+1}. These cavities are formed during the growth of the oxide and their distribution is determined by the local atomic arrangement within a-Al_2O_3. In order to gain more insight into the influence of the porosity of a-Al_2O_3, we investigated the role of O and Al vacancies (V_O and V_{Al}) on the ionic diffusion process. We applied a set of AIMD to these models and extracted the corresponding kinetics

parameters. Figure 7 summarizes the temperature dependence of the diffusion coefficient of Cu^{+1} in presence of V_O and V_{Al}.
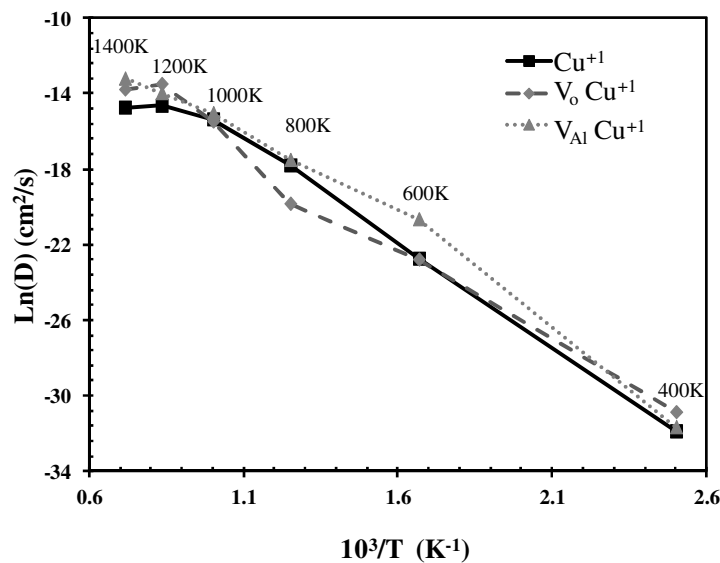
Figure 7. Temperature dependence of the diffusion coefficient of Cu^{+1} in a-Al_2O_3 in presence of V_O (dashed line) and V_{Al} (dotted line).

We find no major impact of the presence of oxygen and aluminum vacancies on the activation energies. However, their introduction increases the kinetic pre-factor by about one order of magnitude (Table III), which suggests a faster diffusion process.

Table III. Computed diffusion coefficient from equation [2] for a Cu^{+1} in a-Al_2O_3 in presence of V_O and V_{Al}.

	D_0 (cm^2/s)	Ea (eV)
Cu^{+1}	5.8×10^{-4}	0.90
V_O	2.2×10^{-3}	0.85
V_{Al}	6.5×10^{-3}	0.90

Interestingly, this implies that the use of an oxygen depletion process, for instance during the deposition of the contact metal electrode, could enhance the diffusion and lead to some undesired overshoot during the filament formation/operation of the CBRAM.

Diffusion of Te ions

Another non negligible contribution to the formation of a low resistance switching filament is the injection of Te ions from the Cu_xTe_{x-1} source as confirmed experimentally by the impact of the thermal treatment on the SIMS profiles of the stack (Figure 8).
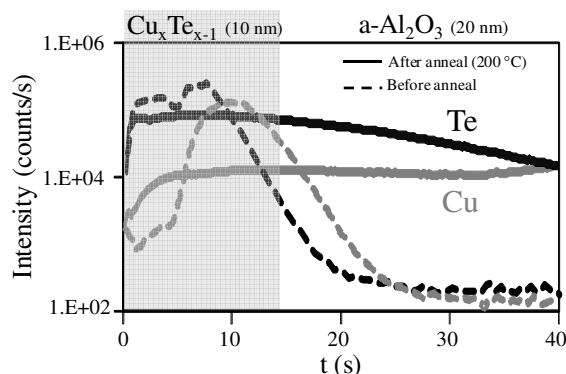
Figure 8. SIMS profile distribution showing a strong presence of Cu (grey line) and Te (black line) in $a-Al_2O_3$ upon an annealing treatment at 200°C in N_2 ambient (solid line) for one hour and before annealing (dashed line). Thickness of 10 (grey region) and 20 nm of Cu_xTe_{x-1} and $a-Al_2O_3$ are used.

Figure 8 shows the SIMS profile obtained before and after annealing treatment at 200°C in a N_2 chamber during 1 hour. Since Te diffuses within the $a-Al_2O_3$ matrix, we also investigated its diffusion kinetics accounting for an oxidation degree (+2). Moreover, we have identified that Te^{+2} could penetrate in $a-Al_2O_3$ together with Cu^{+1} thanks to its exothermicity (Figures 3 and 4). This is in good agreement with the SIMS profile. We used the same procedure as the one carried out for Cu^{+1} and collected the obtained data in Figure 9 and Table IV.
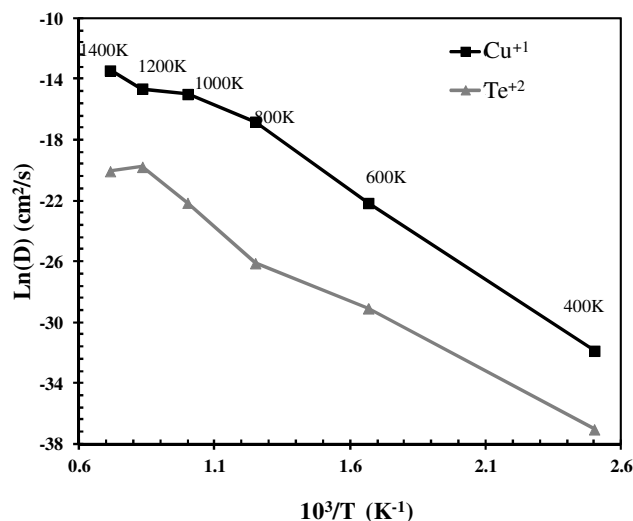
Figure 9. Temperature dependence of the diffusion coefficient of Te^{+2} interstitials in $a-Al_2O_3$ (grey lines) and compared with one of Cu^{+1} (black line).

The distribution of the diffusion coefficient computed for Te^{+2} (grey line) has a similar profile to the one of Cu^{+1} (back line) (Figure 7). Te^{+2} might diffuse in a-Al_2O_3 which is consistent with the evolution of the SIMS profile obtained upon annealing (Figure 8).

Table IV. Computed diffusion coefficient from equation [2] for a Cu^{+1} and Te^{+2} in a-Al_2O_3.

	D_0 (cm^2/s)	Ea (eV)
Cu^{+1}	5.8×10^{-4}	0.90
Te^{+2}	3.4×10^{-6}	0.85

The diffusion of Te^{+2} is associated to an activation energy similar to that of Cu^{+1} but its diffusion pre-factor is about two orders of magnitude lower than the Cu^{+1} one. This suggests that a slower diffusion process occurs for Te^{+2} ions compared to the Cu^{+1} ones. Te^{+2} ions might play a role in the formation of the conductive nanofilament upon the application of a voltage enough high.

Discussions

The analysis of the diffusion kinetics of different oxidation degrees of Cu and Te into a-Al_2O_3 tends to show that both Cu^{+1} or Te^{+2} can contribute to the formation of low resistance nanofilaments. The computation of the injection of the ionized forms of Cu/Te in a-Al_2O_3 indicates that the injection of Cu ions is favored with respect to the Te one (Figures 3 and 4). Therefore, the bridging transport in this CBRAM stack is probably dominated by the migration of Cu^{+1} ions, as validated by Pulse Width electrical measurements (22). The activation energy of the diffusion kinetics of Cu^{+1} in a-Al_2O_3 of 0.9 eV is similar to one reported in literature for Cu in amorphous SiO_2 (23).

The presence of local variations of the atomic density in a-Al_2O_3 and its porosity favor the ionic diffusion process. The atomic vacancies enhance the local Cu^{+1} diffusion by increasing its attempt frequency pre-factor. The presence of a too high concentration of V_O would induce a high diffusivity of Cu^{+1} and might hence affect the stability of the nanofilament and the retention of the memory (2-4). Note that we did not account for the possibility of a combined migration of vacancies and Cu^{+1} ions.

Finally, non linear deviations from the Arrhenius law (Figures 6, 7 and 9) are noticeable due to the stochastic nature of the ionic diffusion (see Figure 5). To minimize their impact, the inclusion of both a large statistical sampling of the diffusion process and longer simulation time is compulsary (but unfortunately computationally untractable).

Summary

An overview of the ionic diffusion process related to the formation of a conductive filament in a CBRAM stack has been presented. Combining the thermodynamics of the injection of Cu and Te ions to their diffusion kinetics, we have investigated the contribution of the dominant ionic species that drive the change in resistance. Although Cu and Te have similar diffusion parameters in a-Al_2O_3, the involvement of Cu^{+1} is advantaged in the formation of the nanofilamemt due to its exothermic character.

References

1. T. Mikolajick, M. Salinga, M. Kund and T. Kever, *Adv. Eng. Mater.* **11**, 235 (2009).
2. M. N. Kozicki, M. Park, and M. Mitkova, *Nanoscale memory elements based on solid-state electrolytes*, IEEE Transactions on Nanotechnology, vol. **2**, pp. 331-8, May (2005).
3. M. Kund, G. Beitel, C.-U. Pinnow, T. Röhr, J. Schumann, R. Symanczyk, K.-D. Ufert and G. Müller, *Conductive bridging RAM (CBRAM): an emerging non-volatile memory technology scalable to sub 20nm*, In Tech. Digest IEDM (2005).
4. N . Banno, T. Sakamoto, T. Hasegawa, K. Terabe, and M. Aono, *Jpn. J. Appl. Phys.* **45(4B)**, 3666–8 (2006).
5. N. Banno , T. Sakamoto , N. Iguchi , H. Sunamura , K. Terabe , T. Hasegawa and M. Aono, *IEEE Trans. Electron Devices* **55**, 3283-7 (2008).
6. T Tsuruoka, K Terabe, T Hasegawa and M Aono, *Nanotechnology* **21**, 425205 (2010).
7. K. Aratani, K. Ohba, T. Mizuguchi, *A novel resistance memory with high scalability and nanosecond switching*, In Tech. Digest IEDM, 783-786 (2007).
8. L. Goux, K. Opsomer, R. Schuitema, R. Degraeve, R. Müller, C. Detavernier, D.J. Wouters, M. Jurczak, L. Altimime and J. A. Kittl, *IEEE Memory Workshop*, 1-4 (2011).
9. R. A. Miron and K. A. Fichthron, *J. Chem. Phys.* **119**, 6210 (2003).
10. R. A. Buckingham, *The Classical Equation of State of Gaseous Helium, Neon and Argon*, Proceedings of the Royal Society of London. Series A, Mathematical and Physical Sciences **168** pp. 264-283 (1938).
11. E. A. Chagarov and A. C. Kummel, Journal of Chemical Physics **130** (12) (2009).
12. J. P. Perdew, K. Burke and M. Ernzerhof, *Phys. Rev. Lett.* **77**, 3865 (1996); **78**, 1396 (E) (1997).
13. D. Vanderbilt, *Phys. Rev. B* **41**, 7892 (1990).
14. S. Baroni, A. Dal Corso, S. de Gironcoli, P. Giannozzi, C. Cavazzoni, G. Ballabio, S. Scandolo, G. Chiarotti, P. Focher, A. Pasquarello, K. Laasonen, A. Trave, R. Car, N. Marzari, A. Kokalj, http://www.pwscf.org/
15. H. Momida, T. Hamada, Y. Takagi, T. Yamamoto, T. Uda and T. Ohno, *Phys. Rev. B* **73**, 054108 (2006).

16. A. M. Goodman, *J. Appl. Phys.* **41**, 2176 (1970).
17. S. Miyaki, *J. Vac. Sci. Technol. B* **19**, 2212 (2001).
18. P. E. Blöchl, *Phys. Rev. B* **62**, 6158 (2000).
19. S. Nosé, *J. Chem. Phys.* **81** (1), 511 (1984).
20. J. Junquera, O. Paz, D. Sánchez-Portal, and E. Artacho, Phys. Rev. B **64**, 235111 (2001).
21. P. Ordejón, E. Artacho, and J. M. Soler, *J. Phys. Rev. B* **53** , R10441 (1996).
22. L. Goux, K. Sankaran, G. Kar, N. Jossart, K. Opsomer, R. Degraeve, G. Pourtois, G.-M. Rignanese, C. Detavernier, S. Clima, Y.-Y. Chen, A. Fantini, B. Govoreanu, D.J. Wouters, M. Jurczak, L. Altimime, J.A. Kittl, *IEEE 2012 Symposia on VLSI Technology and Circuits* (submitted).
23. C. Bo, J. Yan-Hui, L. Gong-Ping and C. Xi-Meng, *Chin. Phys. B* **19**, 026601 (2010).